Temporal evolution of plasma potential in a large-area pulsed dual-frequency inductively coupled discharge

2013 J. Phys. D: Appl. Phys. 46 235203

(http://iopscience.iop.org/0022-3727/46/23/235203)

J. Phys. D: Appl. Phys. **46** (2013) 235203 (9pp) doi:10.1088/0022-3727/46/23/235203

Temporal evolution of plasma potential in a large-area pulsed dual-frequency inductively coupled discharge

Anurag Mishra[1], Jin Seok Seo[1], Kyong Nam Kim[1] and Geun Young Yeom[1,2]

[1] Department of Advanced Materials Science and Engineering, Sungkyunkwan University, Suwon, Gyeonggi-do 440-746, South Korea
[2] SKKU Advanced Institute of Nanotechnology (SAINT), Sungkyunkwan University, Suwon, Gyeunggi-do 440-746, South Korea

E-mail: gyyeom@skku.edu

Received 18 February 2013, in final form 2 April 2013
Published 24 May 2013
Online at stacks.iop.org/JPhysD/46/235203

Abstract

Using an emissive probe technique in 'saturated floating-potential' mode, an investigation of temporal evolution of plasma potential (V_p) in a large-area pulsed dual-frequency (2 MHz/13.56 MHz) inductively coupled plasma (p-DF-CCP) is carried out. The discharge is sustained by an external type ICP antenna at a pressure of 10 mTorr in argon gas environment. The 2 MHz rf is pulsed at a frequency of 1 kHz and a duty ratio of 50%. The emissive probe is located at the centre of the substrate and 20 mm above ($r = 00$ mm and $z = -20$ mm) it. The low-frequency power ($P_{2\,\mathrm{MHz}}$) is varied from 100 to 800 W, whereas the high-frequency power ($P_{13.56\,\mathrm{MHz}}$) from 100 to 700 W.

V_p remains positive during the whole pulse period. The prominent features in the V_p profile remain similar under all operating conditions; however, the magnitude of V_p depends on the applied rf powers. For further investigation, three distinct regions in a typical V_p profile are clearly identified as 'overshoot—immediately after pulse begins', the 'on-time' and the 'off-time'. V_p increases with increasing $P_{13.56\,\mathrm{MHz}}$ and has reverse trend with $P_{2\,\mathrm{MHz}}$.

The electron temperature (T_e) is calculated using the relation between floating potential (V_f) and plasma potential (V_p) for the argon plasma and it is found that T_e increases with increasing $P_{13.56\,\mathrm{MHz}}$ and decreases with $P_{2\,\mathrm{MHz}}$.

It is found that V_p could be modulated using a suitable power combination on two frequencies ($P_{13.56\,\mathrm{MHz}}/P_{2\,\mathrm{MHz}}$).

This paper is an attempt to investigate the time-resolved V_p and T_e with rf powers in a pulsed dual-frequency ICP.

(Some figures may appear in colour only in the online journal)

1. Introduction

Low-temperature plasma processing plays a role in the microelectronics industry for manufacturing various electronic devices such as semiconductor devices, thin-film transistors and liquid crystal displays [1–3]. The process glass size increases continuously and it will be 2200 mm × 2500 mm (eighth generation). Additionally, the semiconductor industry is looking forward to moving for fabrication of electronic devices at a few tens of nanometre level. However, the device fabrication cost increases as the size of the electronic device reduces. For these two reasons (increasing process glass and fabrication of micro-electronic devices at the nanometer level), large-area wafer size is necessary to be adopted in order to improve productivity and optimize the fabrication cost of such microelectronic devices and to give an impetus for developing large-area plasma sources for next-generation microelectronic device fabrication. According to a technology trend forecast, the wafer size will be 450 mm in diameter within a few years [4, 5].

Despite satisfying multiple stringent scaling requirements of micro-electronics fabrication, the most significant challenge for fabrication on a large-area wafer is to precisely control the distribution of plasma species over the substrate. As the wafer size increases and becomes comparable to the wavelength of the applied frequency, a standing wave effect develops and causes strong non-uniformity in the discharge distribution over the wafer area ($\lambda_0 \sim R$, where λ_0 and R are the free space wavelength and the substrate radius, respectively). To satisfy these requirements simultaneously, a significant improvement in controlling key parameters is needed. A cursory literature survey readily reveals that investigations of many types of high-density and large-area plasma sources based on different mechanisms of electromagnetic coupling to the discharge and geometrical configurations have been carried out over the last decade. Various plasma source designs, such as segmented and gridded antennas together with capacitively coupled plasmas (CCPs) [6], have been proposed and implemented to reduce the standing wave effect. Improved radial uniformity has been demonstrated by using C-type ferrite enhancement in inductively coupled plasmas (ICPs) [7]. Various other configurations of plasma sources such as CCPs, very high frequency capacitively coupled plasmas (VHF-CCPs) and ICPs (ferrite core assisted and dual-comb-type antennas) have been proposed and investigated [8–15]. Large-area plasma sources are also important in fusion machines. Recently, an investigation of magnetic field influence on the homogeneity of plasma parameters in a large helium/deuterium ion source relevant for ITER (International Thermonuclear Experimental Reactor) has been carried out [16]. The magnetic field was produced by flowing current in the plasma grid and it was found that plasma homogeneity within 10% near the grid along the direction of magnetic field lines could be achieved. High uniformity was also demonstrated in large-area plasma sources using magnetic multicusp confinement [17].

Distributed helicon sources, electron cyclotron resonance (ECR) and surface wave excited plasma sources have also been investigated [18] in order to achieve large-area plasma sources with enhanced discharge uniformity over the substrate.

Among all the plasma sources, the CCP sources operated at 13.56 MHz were the first to be adopted by the plasma processing industry. Anisotropic etching at the sub-micrometre level requires an ion collisionless sheath in front of the substrate that can be achieved while operating a discharge at a low pressure (<10 mTorr). However, the CCP sources are not able to drive a discharge at low pressures (<10 mTorr) due to the weak rf power coupling to the discharge through sheaths. Operating CCP sources at a very high frequency (typically 2–10 times higher than 13.56 MHz) was proposed to drive these discharges at low pressures (<10 mTorr) [19, 20], however, associated with development of the standing wave effect ($\lambda_0 \sim R$) and strong discharge non-uniformity over the substrate area. Using experimental [21] and computational techniques, it has been demonstrated that the introduction of phase difference (electrical asymmetry) between rf powers applied at top and bottom electrodes could be utilized to control plasma non-uniformity in very-high-frequency CCP discharges [21, 22]. However, the ability of being operated at low pressures due to strong power coupling through an electromagnetic field, a high-density plasma, easier plasma uniformity control, and the separation of discharge production and ion acceleration mechanism of the ICP sources turned the research direction towards developing and investigating the ICP sources for large-area microelectronic device fabrication.

Recently, a novel approach ICP antenna design based on the power splitting mechanism and dual frequency has been proposed [23]. This type of ICP antenna is composed of two co-centric planar coils excited by two different frequencies (2 MHz and 13.56 MHz). It has been demonstrated that a fairly good degree of radial uniformity (∼96%) in discharge distribution over a wafer area of size 450 mm could be achieved. It has also been demonstrated that various discharge parameters such as plasma density, electron temperature, ion and electron energy distribution can be effectively modulated by choosing a particular power ratio ($P_{13.56\,\mathrm{MHz}}/P_{2\,\mathrm{MHz}}$) in the two coils [24, 25]. A further advantage could be added using this antenna with the pulsing technique (as described in [23]). Pulsed plasmas show significant potential to meet the majority of scaling challenges, while leveraging the broad expertise developed over the years in conventional continuous wave (CW) plasma processing. Comprehending the underlying physics and etching mechanisms in pulsed plasma operation is, however, a complex undertaking; hence the full potential of this strategy has not yet been realized. Plasma pulsing allows for better control of ion flux and neutral radical flux to the wafer than for continuous mode, which is key to eliminating several feature profile distortions on the nanometre scale.

Pulsed plasma technologies are among the very few technologies that enable superior control of plasma properties with only a minor change in hardware. Certainly, a pulsed plasma offers new tuning knobs (pulse frequency, duty cycle, and optional phase lag between the source and bias pulses) that enhance independent control of plasma conditions (in particular, ion bombardment energy and plasma chemical composition), otherwise difficult in CW plasmas. Several pulsing modes can be envisaged. For example, either only the source or the bias generator is pulsed, both bias and source are simultaneously pulsed (synchronous pulsing) with or without time delay between them. Since power is actively deposited for only a fraction of time, pulsed plasmas offer the possibility of working with low ion energy regimes (below 5 eV) and with less dissociated (and less reactive) plasmas, resulting in a better process performance in terms of damage, selectivity and profile control.

One of the important discharge parameters is the plasma potential, V_p, in the discharge volume. The spatial distribution of plasma potential determines the electric field that accelerates the electrons to sustain the discharge, and is therefore crucial for discharge formation. On the other hand, the value of plasma potential in front of each electrode, substrate or the wall at a fixed potential determines the sheath potential and therefore ion-bombarding energy with which the ions hit the surface and controls the charged flux to the electrodes. Therefore, knowledge of the temporal evolution of plasma potential is directly linked to dry etching as long as the substrate is not at a floating potential, which adjusts itself

according to the plasma potential and the electron energy. The electron temperature, T_e, is also a very important discharge parameter which, together with plasma density, determines the discharge chemistry and therefore plays a vital role in etching and selectivity. The electron temperature, T_e, determines the ionization, dissociation and excitation rates in the plasma, as well as the energy and ion flux to the substrate. Therefore, information about the temporal evolution of T_e is of considerable importance for understanding the plasma behaviour and optimizing the plasma processes.

In this study, a pulsing scheme (1 kHz and 50% duty ratio) was applied on the inner coil (2 MHz) of the antenna and temporal evolution of the plasma potential was investigated systematically.

2. Emissive probes

Langmuir probes are routinely used to determine V_p in low-temperature plasmas using the following three ways. V_p can be calculated using a conventional Langmuir probe using the following relation [26]:

$$V_p = V_f + \frac{kT_e}{e} \ln\left(\frac{I_{es}}{I_{is}}\right), \quad (1)$$

where k, T_e and e are the Boltzmann constant, electron temperature and elementary charge, respectively. I_{es} is the electron saturation current and I_{is} is the ion saturation current. From equation (1), it is clear that the magnitude of electron saturation current is required to calculate the plasma potential; however, small cylindrical Langmuir probes do not show the electron saturation current region in I–V characteristics as the sheath around the probe increases with probe voltage and makes it difficult to estimate the electron saturation current.

V_p can also be estimated either from the knee in the electron saturation current or from the first or second derivative of the probe I–V characteristic [27]. However, in pulsed plasmas, where the probe sheath potentials change rapidly (faster than the inverse ion plasma frequency), this general technique could be problematic and the measured probe potential cannot keep pace with V_p giving rise to false readings [28]. This situation becomes worse when the probe is used in rf plasmas and even worse in pulsed dual-frequency rf plasmas. A proper rf compensation of Langmuir probe could alleviate this problem; however, small kinks residing on the I–V characteristics due to the pulsed/rf nature of plasmas contribute to false reading of V_p. Also, difficulties arise in plasmas where the electrons are magnetized. Since V_p is determined when the electron random current is drawn to the probe, the local plasma can often become denuded of electrons, hence altering the plasma potential to be measured. However, using an emissive probe, when the probe is electrically floating with no net current drawn from the plasma, to determine V_p can largely overcome these problems. Emissive probes have been proved superior to Langmuir probes, particularly in pulsed plasmas, for determining the plasma potential and have been widely used [29–41]. An emissive probe could be used in three different ways: (a) the 'point of inflection method', (b) the 'diversion method' and (c) the 'saturated floating-potential' method. In this study, the emissive probe is used in the 'saturated floating-potential' mode. The advantage of the method is that it is not necessary to acquire the complete characteristics to obtain the plasma potential; rather it can be accessed from a single measurement of the floating potential, which is easily obtained through a high-impedance measurement against ground. With this measurement being performed with an oscilloscope, a time-resolved determination of varying plasma potentials is possible.

The emissive probe could also be used to estimate the electron temperature using the difference between the floating potentials of the probe when it is cold and under strongly emitting conditions [42, 43]. Therefore, these emissive probe measurements were also used to estimate the time-resolved electron temperature, which was derived from the relation of electron temperature with the plasma and floating potentials.

The working principle of the emissive probe is as follows. In general, the emissive probe consists of a thin, thoriated tungsten wire, which is heated (by passing current through it) up to a temperature until significant thermionic emission of electrons occurs. When the voltage V_b of the biased probe is more negative than V_p these emitted electrons flow from the probe to the plasma, thus reducing the effective net electron flux arriving at the probe. With strong emission this naturally pushes the probe floating potential V_f to more positive values with $V_f \rightarrow V_p$ as the net electron flux balances the ion flux. Typically, there are three methods described in the literature for determining V_p using the emissive probe; these are as follows: the saturated floating probe method in which the voltage at zero probe current is identified as the plasma potential [33]; the divergence point method, in which the point of divergence between 'hot' and 'cold' probe characteristics is taken as the plasma potential [36] and the inflection point method, in which the plasma potential is identified by the inflection point in the 'hot' probe characteristic [37]. In this study, we use the 'floating-point' method (yielding a direct value on an oscilloscope screen), which is valid provided we maintain the probe under full emission conditions during the whole discharge pulse cycle, yielding a temporal resolution below 20 ns. This 'floating-point' method provides an uncertainty in the measurement of V_p with a voltage equivalent of the wire temperature, kT_w/e, which is typically 0.1 V.

3. Experimental details

A schematic of the experimental system is illustrated in figure 1. The anodized aluminum chamber used in this study has a cylindrical geometry with inner diameter of 650 mm and height of 400 mm. A 35 mm thick quartz window is used to cover the top side of the processing chamber and to hold the ICP source, which consists of two spiral coils. The inner coil (thirteen turns) and the outer coil (two turns) are energized by 2 MHz and 13.56 MHz rf powers, by 2 MHz rf (NOVA—50 A, ENI) power and 13.56 MHz rf power (CX-5000 S, COMDEL) via an automatic matching network, respectively. Both rf powers ($P_{2\,MHz}$ and $P_{13.56\,MHz}$) are varied from 100 to 800 W in steps of 100 W. The gases are uniformly distributed

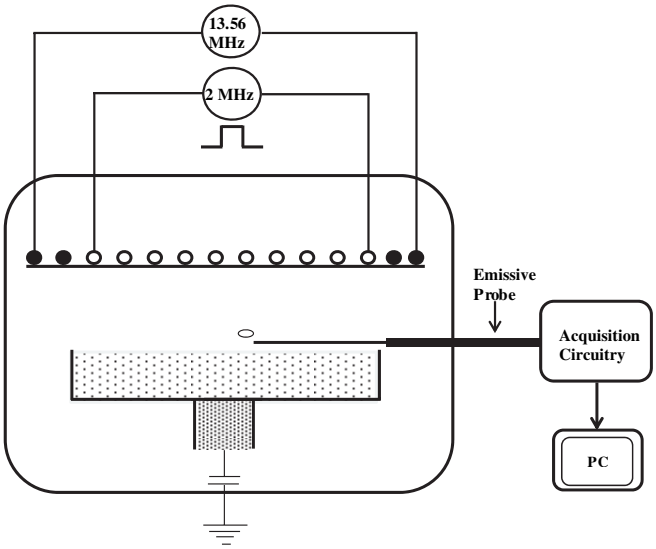

Figure 1. Schematic of the experimental set-up of the pulsed dual-frequency inductively coupled discharge chamber used in this study. The inner coil is energized by pulsed 2 MHz rf power and the outer coil by CW 13.56 MHz rf power.

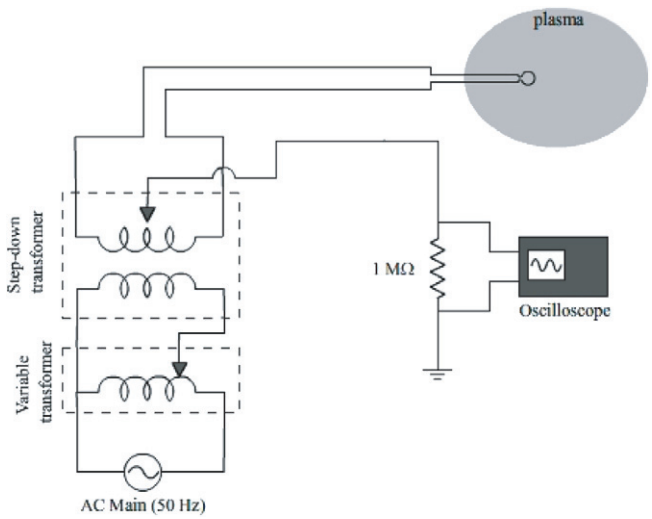

Figure 2. Schematic of the emissive probe electrical arrangement.

inside the chamber via a multi-hole shower head located at the circumference of the vacuum chamber. The separation between the plasma source and the substrate is 130 mm. The chamber walls are electrically grounded. The pressure inside the chamber is controlled using a mass flow controller (2900 series, Tylan) together with an adaptive pressure controller (PM-7, VAT) for the gate valve control. The operating pressure is kept constant at 10 mTorr.

The emissive probe electrical arrangement is shown in figure 2. The emissive probe itself was made of a thoriated tungsten wire of diameter 125 μm, looped in a semicircle of 2 mm diameter and push-fitted into a ceramic stem housing with enamelled copper connecting wires of 250 μm diameter that carry the external heating current. The probe loop was heated by passing a 50 Hz ac current, supplied by a two-stage transformer circuit, through it. The centre tap of the second transformer was connected to a fast oscilloscope (TDS 3014,

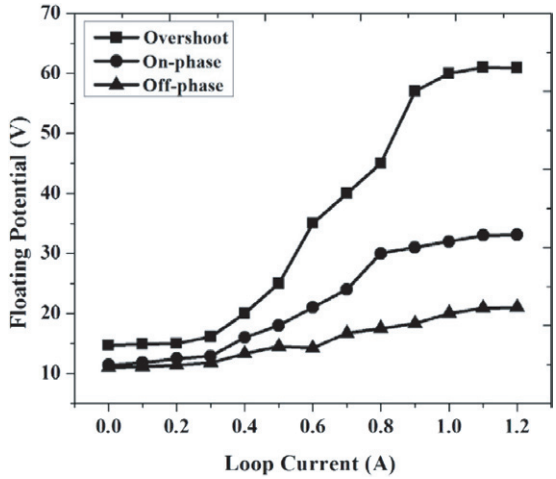

Figure 3. Plot of the measured emissive probe floating potential (V_f) versus loop heat current (I_h) at one position ($r = 00$ mm, $z = -20$ mm) during three identified phases in the V_f waveform: (a) the 'initial overshoot', (b) pulse 'on-time' and (c) pulse 'off-time' as described in figure 7. It should be noted that at $I_L > 1.2$ A, the floating potential V_f approaches the plasma potential V_p. All measurements were carried out at $P_{2\,MHz} = P_{13.56\,MHz} = 100$ W and a pressure of 10 mTorr.

1 MΩ input impedance, Tektronix Ltd) via a single-strand wire (used to minimize the capacitance to ground) to obtain the mean voltage (floating potential) across the loop and hence a good estimate of V_p. This floating-potential data were stored over 128 discharge pulses and then averaged to minimize the random error in the electrical signal.

4. Experimental results and discussion

To ensure that the emissive probe is always under strong emission conditions, a preliminary set of experiments of floating potential versus heating current in the loop are carried out for every condition and the result of such an experiment ($P_{2\,MHz} = P_{13.56\,MHz} = 100$ W) is shown in figure 3. All the V_f values measured during 'on-time' and 'off-time' are measured at 250 and 750 μs after the initiation of the pulse. When the probe is cold ($I_p = 0$ A), the values of V_f for three chosen points (overshoot, on-time, off-time) are 14.7 V, 14 V and 11.4 V, respectively. V_f begins to increase when I_p is 0.4 A and gets saturated at 60.9 V, 33.1 V and 21 V for the three chosen points, respectively, when I_p is 1.2 A. Under this condition, the floating potential measured by the emissive probe is approximately (with an uncertainty of kT_w/e) equal to the plasma potential.

To benchmark emissive probe measurements, the V_f profile was also measured by a non-compensated Langmuir probe under the same conditions and location in the plasma, and is shown in figure 4, together with the same sample by the emissive probe. The values of floating potential were determined by sampling traces directly from the oscilloscope. By comparing two floating-potential samples, figure 4 shows good agreement in transient dynamics except for the fact that the values of V_f are higher for the Langmuir probe due to the difference in measuring techniques used. This

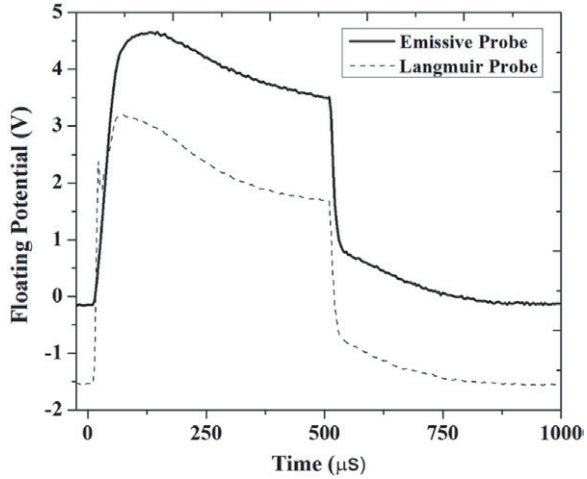

Figure 4. Plot of the measured floating potential by emissive and Langmuir probes. These measurements were carried out at $P_{2\,\mathrm{MHz}} = P_{13.56\,\mathrm{MHz}} = 100$ W, pressure of 10 mTorr and $I_{\mathrm{L}} = 00$ A. The 13.56 MHz rf power was continuous while the 2 MHz rf power was pulsed at 1 kHz and a duty ratio of 50%.

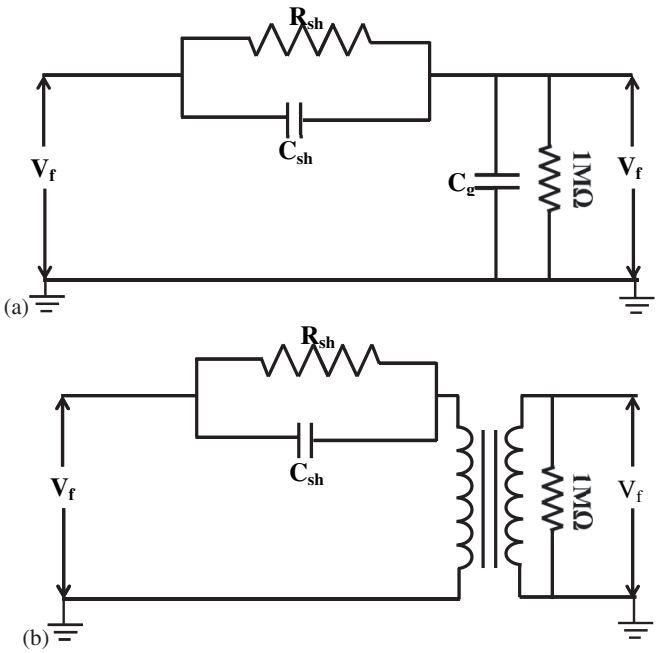

Figure 5. Electrical equivalent circuit of (*a*) Langmuir probe and (*b*) emissive probe used in this study.

could be understood from the electrical equivalent circuits of both probes, as shown in figures 5(*a*) and (*b*). The parallel combination of R_{sh} and C_{sh} is the sheath impedance and C_{g} is a probe to ground capacitance. In both techniques, V_{f} is measured across 1 MΩ (input impedance of the oscilloscope) assuming zero net probe current. For the Langmuir probe measuring circuitry, there is always a very small net probe current flow due to the presence of finite resistance (1 MΩ, oscilloscope input impedance) as it makes the circuit complete. This net flow of probe current elevates the floating potential from its actual values. However, for the emissive probe measuring circuitry, the presence of transformer changes the magnitude of the plasma potential.

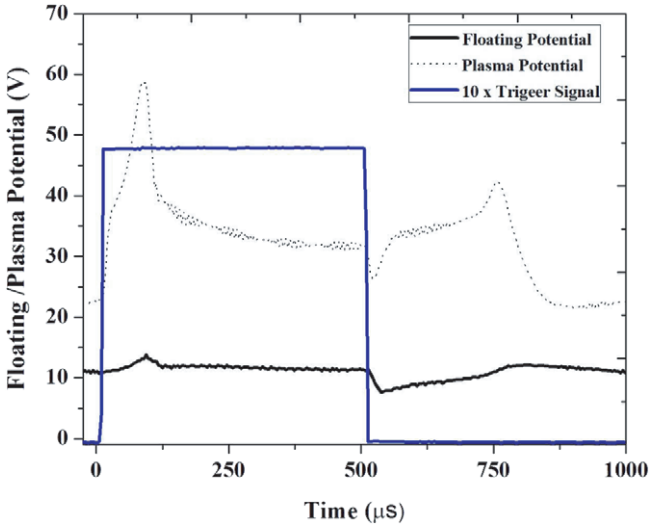

Figure 6. Potential profile measured with the emissive probe for two different conditions: (dotted line) strongly heated at $(r, z) = (0\,\mathrm{mm}, -20\,\mathrm{mm})$, (solid line) no heating at $(r, z) = (0\,\mathrm{mm}, -20\,\mathrm{mm})$. The waveform in blue is for the trigger pulse. The 13.56 MHz rf power was continuous while the 2 MHz rf power was pulsed at 1 kHz and a duty ratio of 50%.

The temporal evolution of V_{p} (under the strong emission condition) and V_{f} (under the zero emission condition) acquired by the emissive probe, measured at powers of $P_{2\,\mathrm{MHz}} = P_{13.56\,\mathrm{MHz}} = 100$ W, and an average pressure of 10 mTorr, is shown in figure 6. The emissive probe was located at a particular position of the substrate ($r = 0$ mm and $z = 20$ mm). V_{p} gets a significant spike of ∼60 V at the beginning of the pulse, ∼90 μs after the initiation of the rf pulse and this time lag decreases with increasing rf powers. This time lag is mainly due to a statistical time lag for electrons to develop an avalanche and finally a plasma. Another contribution to this time lag, however small, comes from a finite time (∼8 μs) taken by the TTL trigger signal to reach its peak value. Subsequently, the plasma potential decreases sharply and later on, after $\sim t = 120\,\mu$s, attains a stable value of ∼38 V for the rest of the pulse 'on-time'. As the pulse is switched off, the plasma potential gets a small dip of ∼27 V (at $t = 521\,\mu$s) and gets a relatively stable value of ∼34 V for the rest of the pulse 'off-time'. This high value of plasma potential during pulse 'off-time' is interesting and is attributed to the dominant effects of 13.56 MHz power in pulse 'off-time'. It will be discussed in detail later.

For an in-depth analysis, three features on the V_{p} profile were clearly identified as an 'initial overshoot' (within a few tens of μs after the initiation of the pulse), a relatively stable 'on-time' (∼100 μs after the initiation of the pulse) and a stable 'off-time' (∼30 μs after switching off the pulse), as shown in figures 7(*a*)-(*d*).

Figure 7(*a*) shows the V_{p} profile at $P_{2\,\mathrm{MHz}} = 100$ W and with $P_{13.56\,\mathrm{MHz}}$ varied from 100 to 800 W at an average pressure of 10 mTorr. It can be seen in figure 7(*a*) that there is an initial overshoot as the pulse is switched on. This peak value of this initial overshoot depends on $P_{13.56\,\mathrm{MHz}}$. The zoomed-in plot of the initial overshoot is shown in figure 7(*b*) and it is clear that the peak value of the initial overshoot increases

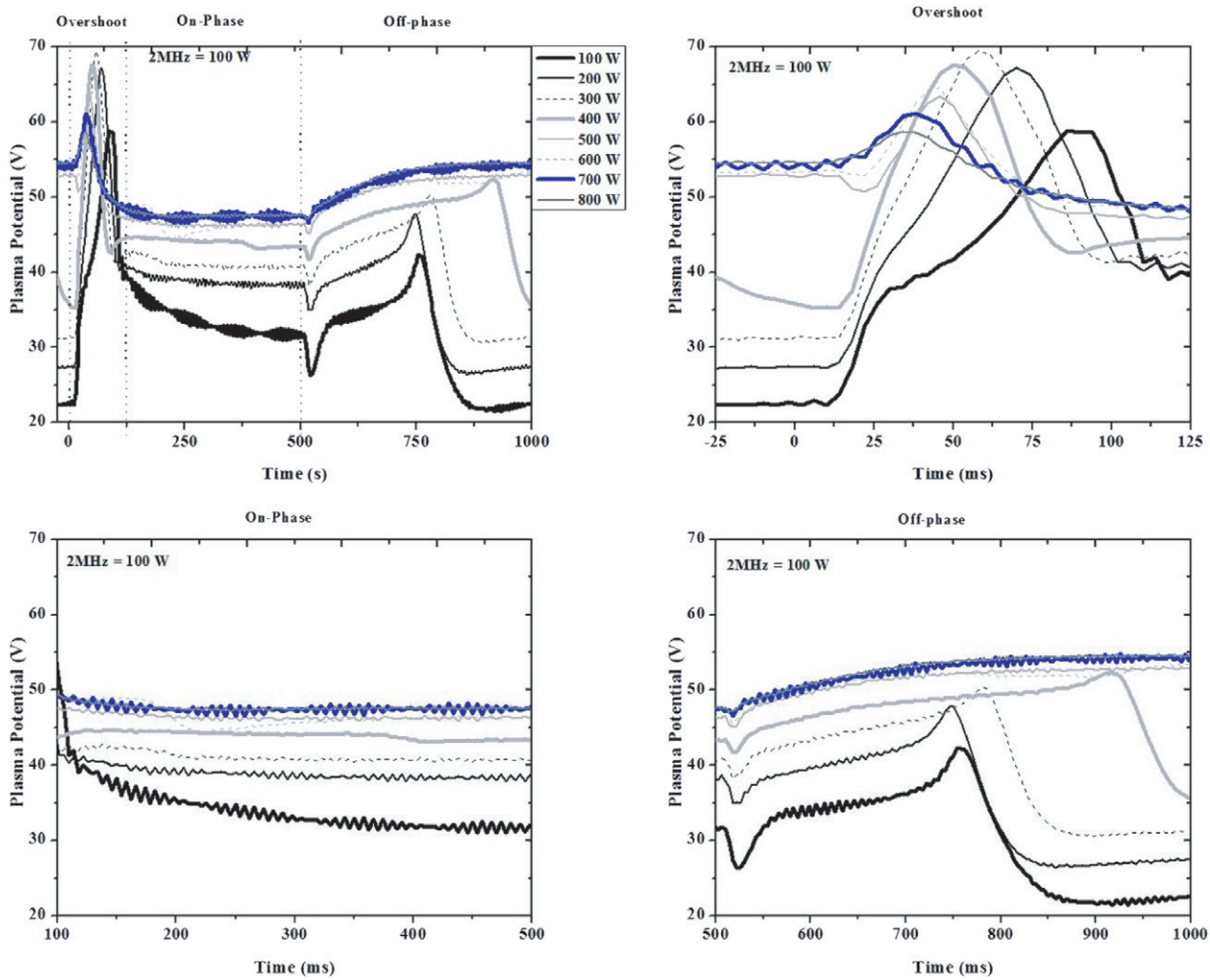

Figure 7. Potential profile measured with the emissive probe (*a*) for eight different $P_{13.56\,\mathrm{MHz}}$ at an average pressure of 10 mTorr, (*b*) zoomed-in overshoot phase, (*c*) zoomed-in pulse 'on-time' and (*d*) zoomed-in pulse 'off-time'. The 13.56 MHz rf power was continuous while the 2 MHz rf power was pulsed at 1 kHz and a duty ratio of 50%. The value of $P_{2\,\mathrm{MHz}}$ was 100 W.

with $P_{13.56\,\mathrm{MHz}}$ up to 300 W and then decreases. Another interesting feature observed is that the time to achieve the peak value of overshoot decreases with increasing $P_{13.56\,\mathrm{MHz}}$. This decreasing statistical time lag (time difference between the initiation of the discharge pulse and the time of the initial peak) depends on the background plasma density. As $P_{13.56\,\mathrm{MHz}}$ increases, the pulse (2 MHz) sees a higher background plasma density and therefore takes less time to have an electron avalanche and then finally a plasma. After $\sim$120 μs from the initiation of the pulse, V_p gets a stable value, within a few volts, during the rest of the pulse 'on-time'. The important feature observed during the pulse 'on-time' is that the V_p values increase with $P_{13.56\,\mathrm{MHz}}$. It can be understood as follows. The plasma potential can be determined from Poisson's relation

$$\varepsilon_0 \cdot \Delta V_\mathrm{p}(r) = e[n_\mathrm{e}(r) - n_\mathrm{i}(r)], \qquad (2)$$

where ε_0 is the dielectric constant, e is the electronic charge, n_e is the electron density, n_i is the positive ion density and r is for a particular spatial location. Figure 8 shows the effect of $P_{13.56\,\mathrm{MHz}}$ on the plasma potential at $P_{2\,\mathrm{MHz}} = 400$ W. The plasma potential increases with $P_{13.56\,\mathrm{MHz}}$. This could be understood as follows. Increasing $P_{13.56\,\mathrm{MHz}}$ levels increases the plasma density at the edge of the discharge (location of 13.56 MHz coil) and thus provides a lower impedance path to the grounded chamber walls for electrons. Additionally, increasing $P_{13.56\,\mathrm{MHz}}$ also increases the electron temperature (see figure 13), i.e. random thermal motion of electrons. Both these processes facilitate the electron motion towards the grounded walls and therefore increase the right-hand side of equation (2). The result is increased plasma potential, as observed in this study. The same behaviour of plasma potential is also seen during the pulse 'off-time'. Interestingly, the plasma potential begins to decrease at a considerably long time (at $t =\sim 750\,\mu$s, for $P_{13.56\,\mathrm{MHz}} = 100$ W) after the pulse is switched off and it increases with increasing $P_{13.56\,\mathrm{MHz}}$, as shown in figure 9. Beyond $P_{13.56\,\mathrm{MHz}} = 400$ W, the plasma potential is almost constant for the entire pulse 'off-time'. To identify the exact reason for this observation further investigations of plasma parameters (that we wish to carry out by time-resolved Langmuir probe measurements) are required; however, it could be attributed to the background plasma density and electron temperature caused by CW $P_{13.56\,\mathrm{MHz}}$.

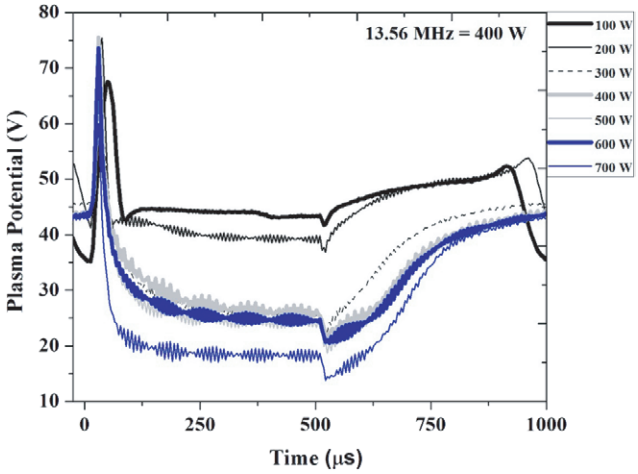

Figure 8. Potential profile measured at seven different values of $P_{2\,\mathrm{MHz}}$. $P_{13.56\,\mathrm{MHz}}$ is kept constant at 400 W. These measurements were carried out at a pressure of 10 mTorr and at the centre of the discharge. The 13.56 MHz rf power was continuous while the 2 MHz rf power was pulsed at 1 kHz and a duty ratio of 50%.

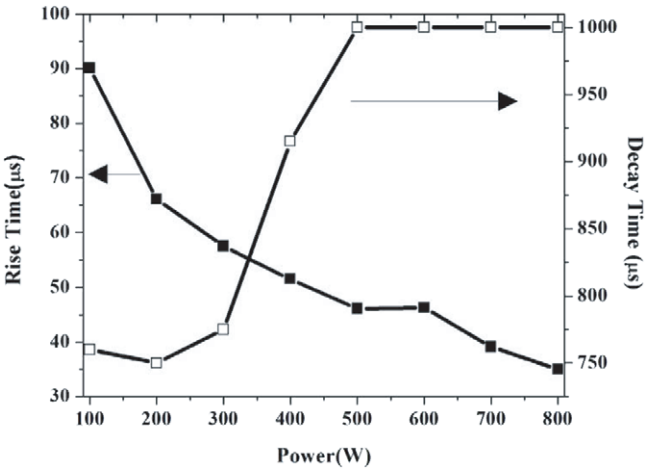

Figure 9. Plot of time to achieve the peak potential during the overshot phase and time of dropping of potential in the pulse 'off-time' phase. The time is shown as solid rectangles while decay time as empty rectangles. These measurements were carried out at $P_{2\,\mathrm{MHz}} = P_{13.56\,\mathrm{MHz}} = 100$ W and a pressure of 10 mTorr. The 13.56 MHz rf power was continuous while the 2 MHz rf power was pulsed at 1 kHz and a duty ratio of 50%.

High level of $P_{13.56\,\mathrm{MHz}}$ produces a higher plasma density and a higher electron temperature which, in turn, results in an electron flow towards the grounded wall and therefore shows a high plasma potential during the pulse 'off-time'.

The temporal evolution of plasma potential with $P_{13.56\,\mathrm{MHz}}$ at higher values of $P_{2\,\mathrm{MHz}}$ has similar trends; however, the magnitude of plasma potential decreases with increasing $P_{2\,\mathrm{MHz}}$. Figure 10 shows the variation in the temporal profile of V_p with $P_{2\,\mathrm{MHz}}$ at $P_{13.56\,\mathrm{MHz}} = 400$ W and it is clear from this figure that V_p decreases with increasing $P_{2\,\mathrm{MHz}}$. This observation is common in glow discharges and is due to the increase in two-step ionization at higher plasma densities (higher rf powers).

The temporal evolution of electron temperature is qualitatively estimated using the relation between plasma

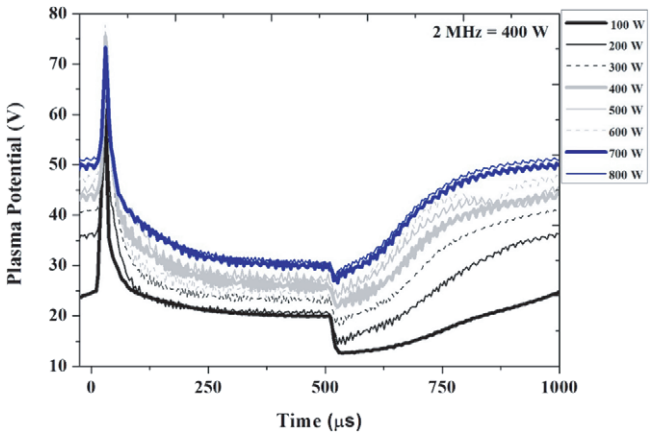

Figure 10. Potential profile measured at seven different values of $P_{13.56\,\mathrm{MHz}}$. $P_{2\,\mathrm{MHz}}$ is kept constant at 400 W. These measurements were carried out at a pressure of 10 mTorr and at the centre of the discharge. The 13.56 MHz rf power was continuous while the 2 MHz rf power was pulsed at 1 kHz and a duty ratio of 50%.

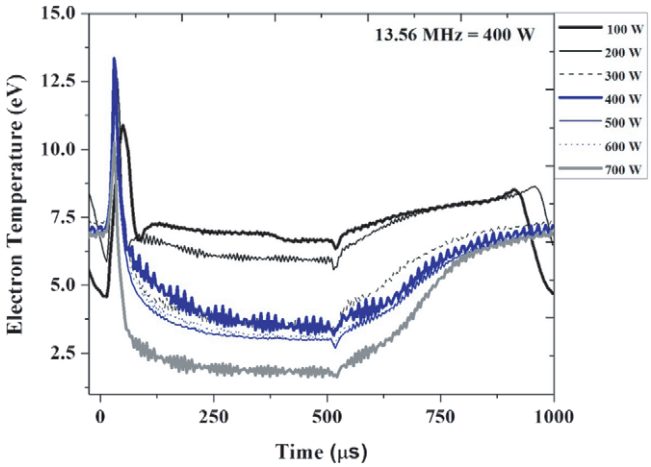

Figure 11. Electron temperature profile, calculated from the relation between plasma potential and floating potential at seven different values of $P_{2\,\mathrm{MHz}}$. $P_{13.56\,\mathrm{MHz}}$ is kept constant at 400 W. These measurements were carried out at a pressure of 10 mTorr and at the centre of the discharge. The 13.56 MHz rf power was continuous while the 2 MHz rf power was pulsed at 1 kHz and a duty ratio of 50%.

potential and floating potential [44]:

$$V_\mathrm{p} - V_\mathrm{f} = \frac{KT_\mathrm{e}}{2e} \ln\left(\frac{\pi m}{2M}\right), \tag{3}$$

where V_p and V_f are the plasma and floating potentials, T_e is the electron temperature, m is the electronic mass and M is the atomic mass of the discharge gas. Thus calculated, $(V_\mathrm{p} - V_\mathrm{f})$ is 5.38 for argon gas. Electron temperature profiles thus derived are shown in figures 11 and 12 for $P_{2\,\mathrm{MHz}} = 400$ W and $P_{13.56\,\mathrm{MHz}} = 400$ W, respectively. An analysis of figure 11 readily reveals that the effect of increasing $P_{2\,\mathrm{MHz}}$ is to lower the electron temperature. The electron temperature decreases with applied 2 MHz rf pulse power during all the three chosen phases. T_e decreases from ~7.5 to ~2 eV during the stable 'on-time' when the pulse power is varied from 100 to 700 W. During the 'off-time', it decreases from ~7.7 to ~5 eV at $t = 750\,\mu$s.

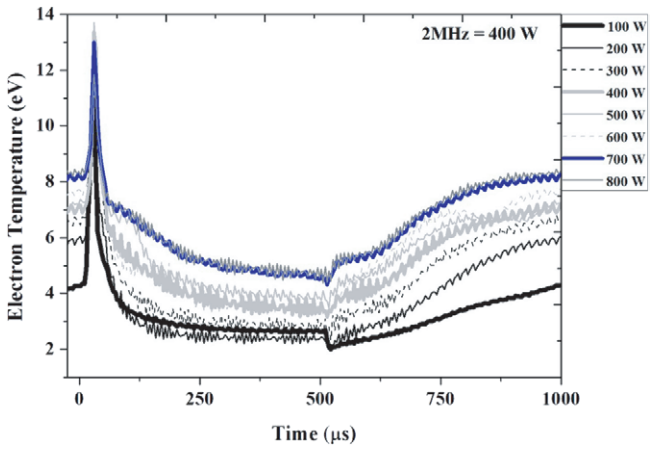

Figure 12. Electron temperature profile, calculated from the relation between plasma potential and floating potential at seven different values of $P_{13.56\,\mathrm{MHz}}$. $P_{2\,\mathrm{MHz}}$ is kept constant at 400 W. These measurements were carried out at a pressure of 10 mTorr and at the centre of the discharge. The 13.56 MHz rf power was continuous while the 2 MHz rf power was pulsed at 1 kHz and a duty ratio of 50%.

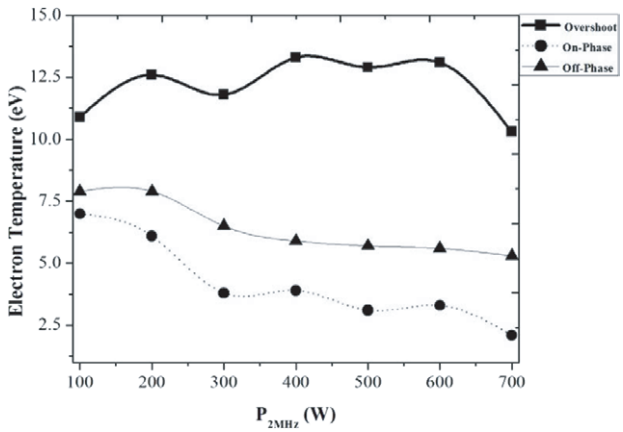

Figure 13. Plot of electron temperature variation with $P_{2\,\mathrm{MHz}}$ while $P_{13.56\,\mathrm{MHz}}$ is kept constant at 400 W. These measurements were carried out at a pressure of 10 mTorr and at the centre of the discharge. The 13.56 MHz rf power was continuous while the 2 MHz rf power was pulsed at 1 kHz and a duty ratio of 50%.

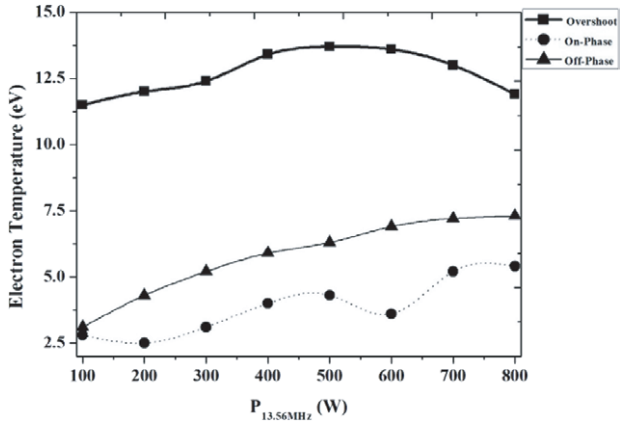

Figure 14. Plot of electron temperature variation with $P_{13.56\,\mathrm{MHz}}$, while $P_{2\,\mathrm{MHz}}$ is kept constant at 400 W. These measurements were carried out at a pressure of 10 mTorr and at the centre of the discharge. The 13.56 MHz rf power was continuous while the 2 MHz rf power was pulsed at 1 kHz and a duty ratio of 50%.

However, the effect of increasing $P_{13.56\,\mathrm{MHz}}$ on the electron temperature is the reverse, as shown in figure 12. T_e increases from ~2.5 to ~6 eV during the pulse 'on-time' when $P_{13.56\,MHz}$ is increased from 100 to 800 W.

In addition to the general features observed in T_e evolution (figures 11 and 12), some structures during off-time, particularly at high powers (500 W), are also observed. As the electron temperatures are calculated from the plasma potential profile, there is a finite possibility of inclusion of errors associated with the emissive probe technique. Therefore, the structure observed in temporal dependence of electron temperature could be explained by the basic operating mechanism of the emissive probe.

Moreover, the emissive probe technique in the floating mode gives only a qualitative insight into the temporal evolution of T_e. For quantitative accuracy, the discharge should be characterized with other techniques such as the Langmuir probe.

To get a better insight into the electron temperature variation with $P_{2\,\mathrm{MHz}}/P_{13.56\,\mathrm{MHz}}$, the electron temperature in the three identified regions is plotted with increasing $P_{2\,\mathrm{MHz}}$ ($P_{13.56\,\mathrm{MHz}} = 400$ W) and $P_{13.56\,\mathrm{MHz}}$ ($P_{2\,\mathrm{MHz}} = 400$ W), as shown in figures 13 and 14, respectively. From figure 13, it can be seen that the electron temperature is almost constant within the range ± 1 eV during the initial overshoot; however, it has a decreasing trend with $P_{2\,\mathrm{MHz}}$ during the 'on-time' and 'off-time'. Figure 14 shows the electron temperature variation with $P_{13.56\,\mathrm{MHz}}$ at a fixed value of $P_{2\,\mathrm{MHz}}$. It is found that the electron temperature increases with $P_{13.56\,\mathrm{MHz}}$ in all three regions.

5. Conclusions

An experimental study is carried to investigate the temporal evolution of plasma potential in a large-area pulsed dual-frequency ICP source. The diagnostic technique used is the emissive probe in the 'saturated floating-potential mode'. It is observed that the plasma potential remains positive for the whole cycle under all conditions. There is a finite time lag between the initiation of the discharge pulse and the time of occurrence of the peak in the initial overshoot region and it is attributed to the background plasma. This time lag decreases with increasing $P_{2\,\mathrm{MHz}}/P_{13.56\,\mathrm{MHz}}$.

The effect of increasing $P_{2\,\mathrm{MHz}}$ is to lower the plasma potential; however, increasing $P_{13.56\,\mathrm{MHz}}$ increases the plasma potential. The interesting feature observed is that the plasma potential can be modulated during the pulse 'off-time' by varying $P_{2\,\mathrm{MHz}}/P_{13.56\,\mathrm{MHz}}$.

The electron temperature is also calculated using the relation between plasma potential and floating potential. It is found that the effect of increasing $P_{2\,\mathrm{MHz}}$ is to lower the electron temperature; however, increasing $P_{13.56\,\mathrm{MHz}}$ increases the electron temperature.

Acknowledgments

This work was supported by the IT R&D Industrial Strategic Technology development program (10041926, Development

of high density plasma technologies for thin film deposition of nanoscale semiconductor and flexible display processing) and (KI002182, TFT backplane technology for next generation display) funded by the Ministry of Knowledge Economy (MKE, Korea). This work was supported in part by the World Class University program of National Research Foundation of Korea (Grant No R32-10124).

References

[1] Chang C Y and Sze S M 1996 *ULSI Technology* (New York: McGraw-Hill) p 329
[2] Hopwood J 1992 *Plasma Sources Sci. Technol.* **1** 109
[3] Kahoh M, Suzuki K, Tonotani J, Aoki K and Yamage M 2001 *Japan. J. Appl. Phys. Part 1* **40** 5419
[4] 2009 *International Technology Roadmap for Semiconductor* 2009 edn www.itrs.net
[5] Collision W Z, Ni T Q and Barnes M S 1998 *J. Vac. Sci. Technol.* A **16** 100
[6] Yang Y and Kushner M J 2010 *J. Appl. Phys.* **108** 113306
[7] Hong S P, Lim J H, Gweon G H and Yeom G Y 2010 *Japan. J. Appl. Phys.* **49** 080217
[8] Kim K N, Lim J H, Yeom G Y, Lee S H and Lee J K 2006 *Appl. Phys. Lett.* **89** 251501
[9] Gweon G H, Lim J H, Kim K N, Hong S P, Min T H and Yeom G Y 2010 *Vacuum* **84** 823
[10] Lim J H, Kim K N, Gweon G H, Park J B and Yeom G Y 2009 *Plasma Chem. Plasma Process.* **29** 251
[11] Kim K N, Lim J H and Yeom G Y 2009 *Japan. J. Appl. Phys.* **48** 116006
[12] Kim K N, Lim J H, Lim W S and Yeom G Y 2010 *IEEE Trans. Plasma Sci.* **38** 133
[13] Lim J H, Kim K N, Park J K, Lim J T and Yeom G Y 2008 *Appl. Phys. Lett.* **92** 051504
[14] Setsuhara Y, Takenaka K, Nishisaka K and Ebe A 2007 *Plasma Process Polym.* **4** S628
[15] Lim J H, Kim K N and Yeom G Y 2007 *Plasma Process Polym.* **4** S999
[16] Schiesko L, Franzen P and Fantz U 2012 *Plasma Sources Sci. Technol.* **21** 065007
[17] Biloiu C, Olson J C, Scheuer J T and Renau A 2011 *IEEE Trans. Plasma Sci.* **39** 2456
[18] Chen F F and Chang J P 2002 *Lecture Notes on Principles of Plasma Processing* (Dordrecht/New York: Kluwer/Plenum)
[19] Lieberman M A, Booth J P, Chabert P, Rax J M and Turner M M 2002 *Plasma Sources Sci. Technol.* **11** 283
[20] Chabert P 2007 *J. Appl. Phys. D:Appl. Phys.* **40** R63
[21] Volynets V, Shin H, Kang D and Sung D 2010 *J. Phys. D: Appl. Phys.* **43** 085203
[22] Bera K, Rauf S and Collins K 2008 *IEEE Trans. Plasma Sci.* **36** 1366
[23] Mishra A, Kim K N, Kim T H and Yeom G Y 2012 *Plasma Source Sci. Technol.* **21** 035018
[24] Mishra A, Kim T H, Kim K N and Yeom G Y 2012 *J. Phys. D: Appl. Phys.* **45** 475201
[25] Mishra A, Kim T H, Kim K N and Yeom G Y 2013 *Plasma Sources Sci. Technol.* **22** 015022
[26] Rauch A, Mendelsberg R J, Sanders J M and Anders A 2012 *J. Appl. Phys.* **111** 083302
[27] Chen F F 1965 *Plasma Diagnostics Techniques* ed R H Huddlestone and S L Leonard (New York: Academic) chapter 4
[28] Karkari S K, Vetushka A and Bradley J W 2003 *J. Vac. Sci. Technol.* A **21** L28
[29] Bradley J W, Thompson S and Gonzalvo Y A 2001 *Plasma Sources Sci. Technol.* **10** 490
[30] Bradley J W, Karkari S K and Vetushka A 2004 *Plasma Sources Sci. Technol.* **13** 189
[31] Hershkowitz N, Nelson B, Pew J and Gates D 1983 *Rev. Sci. Instrum.* **54** 29
[32] Iizuka S *et al* 1981 *J. Phys. E: J. Sci. Instrum.* **14** 1291
[33] Kemp R F and Sellen J J M 1966 *Rev. Sci. Instrum.* **37** 455
[34] Mahdizadeh N *et al* 2005 *Plasma Phys. Control. Fusion* **47** 569–779
[35] Pickova I, Marek A, Tichy M, Kudrna P and Apetrei R 2006 *Czech. J. Phys.* **56** B1002
[36] Smith J R, Hershkowitz N and Coakley P 1979 *Rev. Sci. Instrum.* **50** 210
[37] Wang E Y, Intrator T and Hershkowitz N 1985 *Rev. Sci. Instrum.* **56** 519
[38] Sheehan J P, Raitses Y, Hershkowitz N, Kaganovich I and Fisch N J 2011 *Phys. Plasmas* **18** 073501
[39] Mishra A, Kelly P J and Badley J W 2010 *Plasma Sources Sci. Technol.* **19** 045014
[40] Mishra A, Kelly P J and Badley J W 2011 *J. Phys. D: Appl. Phys.* **44** 425201
[41] Mishra A, Jeon M W, Kim K N and Yeom G Y 2012 *Plasma Sources Sci. Technol.* **21** 055006
[42] Raitses Y, Staack D, Smirnov A and Fisch N J 2005 *Phys. Plasmas* **12** 073507
[43] Schrittwieser R, Ionita C, Balan P, Silva C, Figueiredo H, Varandas C A F, Rasmussen J J and Naulin V 2008 *Plasma Phys. Control. Fusion* **50** 055004
[44] Chen F F and Cahng J P 1970 *Principles of Plasma Processing* (Dordrecht/New York: Kluwer/Plenum)